Simultaneous Calibration of ALS Systems and Alignment of Multiview LiDAR Scans of Urban Areas

Marcus Hebel and Uwe Stilla, *Senior Member*, IEEE

Abstract—Tasks such as city modeling or urban planning require the registration, alignment, and comparison of multi-view and/or multi-temporal remote sensing data. ALS (airborne laser scanning) is one of the established techniques to deliver these data. Regrettably, direct georeferencing of ALS measurements usually leads to considerable displacements that limit connectivity and/or comparability of overlapping point clouds. Most reasons for this effect can be found in the impreciseness of the positioning and orientation sensors and their misalignment to the laser scanner. Typically, these sensors are comprised of a GNSS (global navigation satellite system) receiver and an IMU (inertial measurement unit). This paper presents a method for the automatic self-calibration of such ALS systems and the alignment of the acquired laser point clouds. Although applicable to classical nadir configurations, a novelty of our approach is the consideration of multiple data sets that were recorded with an oblique forward-looking full-waveform laser scanner. A combination of a region-growing approach with a RANSAC (random sample consensus) segmentation method is used to extract planar shapes. Matching objects in overlapping data sets are identified with regard to several geometric attributes. A new methodology is presented to transfer the planarity constraints into systems of linear equations to determine both the boresight parameters and the data alignment. In addition to system calibration and data registration, the presented workflow results in merged 3D point clouds that contain information concerning rooftops and all building facades. This database represents a solid basis and reference for applications such as change detection.

Index Terms—Airborne laser scanning, boresight calibration, data alignment, registration, urban areas

I. INTRODUCTION

A. Problem description

Airborne laser scanning (ALS) usually combines a LiDAR (light detection and ranging) device with high-precision navigational sensors mounted on an aircraft. Typically, an IMU (inertial measurement unit) and a GNSS receiver (global navigation satellite system, e.g., GPS, the Global Positioning System) are operated synchronously with a LiDAR scanning mechanism. Range values are derived from measuring the time-of-flight of single laser pulses, and scanning is performed by one or more deflection mirrors in combination with the forward moving aircraft. The navigational sensors are used to obtain 3D points associated with the range measurements, resulting in a georeferenced point cloud of the terrain. A good overview and thorough description of ALS principles can be found in [1].

Currently available laser scanners are capable of acquiring the full waveform of reflected pulses, thus enabling new methods of data analysis [2]-[4]. Multiple range values can be obtained if echoes are received from different objects within the laser footprint. Additional attributes such as echo width and amplitude can be derived from waveform analysis to support the classification of objects. A well-established application of ALS data acquired in urban areas is the generation of 3D city models. However, the overall quality of the derived city model depends greatly on the accuracy of the data input, which is directly dependent on the precision of the navigational information. In this context, the use of one or more GNSS ground reference stations is required, as is the global optimization of the GNSS/IMU trajectory data [5].

During ALS data acquisition, laser range measurements are transferred to geographic coordinates with regard to current position/orientation of the laser scanner and the angle of the deflection mirrors. This process is usually referred to as direct georeferencing. Despite careful and accurate assembling of the sensor system, direct georeferencing commonly results in considerable displacements between overlapping strips. Sources of errors can be found, for instance, in the accuracy of the GNSS data, the sensor synchronization, or the control of the scanning mirrors. In this paper, we focus mainly on the automatic determination of the system's boresight parameters, i.e., the alignment of the laser scanner to the navigational sensors. In addition to system calibration, we minimize remaining displacements by an object-based registration of overlapping parts of the ALS data sets.

Airborne laser scanning for geodetic applications is usually accomplished in the nadir view. This configuration reduces occlusions when scanning bare earth or roof landscapes in urban areas, but it leads to missing structures in the data, e.g., facades of buildings and areas under bridges or roofed

M. Hebel is with the Fraunhofer Institute of Optronics, System Technologies and Image Exploitation IOSB, 76275 Ettlingen, Germany (phone: +49-7243-992-323; e-mail: marcus.hebel@iosb.fraunhofer.de).

U. Stilla is with the Institute for Photogrammetry and Cartography, Technische Universitaet Muenchen, 80290 Muenchen, Germany (e-mail: stilla@tum.de).

shelters. These data can be complemented, e.g., by the use of terrestrial laser scanning (TLS). An alternative to close the gap between missing structures in classical nadir data and terrestrial data is to capture the scene with an oblique-looking airborne sensor. Obviously, this approach requires criss-crossing flight lines instead of a classical parallel pattern. As an advantage, merging of all views results in a point cloud that contains information concerning all facades of buildings. In addition to 3D city modeling, such point clouds provide an ideal basis for change detection in urban areas. Moreover, an oblique forward-looking ALS configuration and real-time data analysis are ideally suited to support helicopter pilots during their missions, e.g., with obstacle warnings and terrain-referenced navigation. Similar to multi-aspect data acquisition, multi-temporal comparison also requires the best possible data registration and fitting accuracy.

B. Related work

In the last two decades, registration of point clouds and calibration of airborne laser scanning systems have been explored by various scientists. These two topics are inherently different. On one hand, considering only the alignment of given point clouds ignores the circumstances of data acquisition and tries to optimize the data in itself. On the other hand, ALS calibration aims at the optimization of the sensor parameters such that the overall accuracy of fit is implicitly improved. In this paper, we address the calibration of such ALS systems that allow access to the component's raw measurements (e.g., the GNSS/IMU trajectory). Another group of registration methods can be found in literature that attempt to recover and adjust the settings even in cases where this information is missing.

Some procedures described in this paper are concerned with the segmentation of point clouds into planar surfaces. Many different methods regarding this topic can be found in the literature. In addition, some authors are also interested in detecting spheres, cylinders, or cones. Rabbani et al. described two methods for the registration of point clouds where they fitted models to the data by analyzing least-squares quality measures [6]. Vosselman et al. used a 3D Hough transform to recognize structures in point clouds [7]. The RANSAC algorithm [8] offers several advantages to exploit for point-cloud shape detection [9]. Similar to Sampath and Shan [10], we begin our approach with a local principal component analysis [11]. After that, we apply an iterative combination of a RANSAC-based robust estimation technique with a region growing approach to identify planar patches in the point cloud data. The number of outliers allows us to distinguish between buildings and irregularly-shaped objects such as trees.

Different measures of data quality have been proposed to evaluate the accuracy of (overlapping) ALS point clouds. As the precision of dynamic ALS data acquisition is affected by many influencing factors, most quality criteria directly originate in the data. Maas, for instance, implemented a least-squares matching on a TIN structure to determine strip discrepancies [12]. Ressl et al. first interpolated a DEM (digital elevation model) for each strip. After that, attributes derived from the difference of these DEMs act as a quality measure for the given ALS data [13]. Vosselman used automatically extracted ridge lines of buildings to analyze the planimetric accuracy of ALS point clouds acquired in urban areas [14]. Kager used distances between homologous planar objects to evaluate the accuracy of ALS data [15]. Habib et al. even detected systematic errors by analyzing consistent incompatibilities between conjugate surface elements [16]. Similar to Soudarissanane et al. [17], we assess point-to-surface distances in overlapping parts of point clouds, taking into account that the computation of local normal directions is part of our workflow.

Since Besl and McKay proposed their iterative-closest-point (ICP) algorithm [18], this approach has become the standard solution to the point-set registration problem. During an ICP operation, a data shape D is moved iteratively to be in best alignment with a model M. In particular, a translation and a rotation are identified to move the data points towards the closest model points in a way that the average Euclidean distance is minimized. This problem can be solved explicitly, and it has been shown by Besl and McKay that the iterative procedure converges to a local minimum of the error function. Many different attempts have been made to improve the classical ICP algorithm [19]. A comparison of several variants has been given by Rusinkiewicz and Levoy [20]. In the context of ALS data correction, the main disadvantages of ICP-based registration methods are as follows: (1) the absolute accuracy remains vague because one data set is kept unchanged and all other point clouds are drawn on it, and (2) the application of the ICP algorithm presumes a rigid transformation to be sufficient to solve the registration problem. Actually, this assumption is incorrect for a misadjusted ALS sensor system.

In adverse cases, existing 3D point clouds are nonlinearly distorted by calibration errors, but parameters of direct georeferencing have not been stored. Methods to improve data quality in such situations have been proposed by Ressl et al. [21] and Habib et al. [22]. If laser range measurements, scanning parameters, and the GNSS/IMU trajectory are available, such as in our case, these data can be exploited to determine the ALS mounting errors [23]. Skaloud and Lichti approached this problem with a rigorous method to estimate the system calibration parameters such that 3D points representing a plane are conditioned to show best possible planarity [24]. Their boresight calibration method is applicable to single strips, requiring manual selection of surfaces with known characteristics in the data. An extension of this method to multiple flight lines in urban terrain is described in [25]. The automated detection of roofs within a reference strip is followed by a local search for corresponding objects in overlapping parts of the other strips. Planar features are also commonly used in software for automatic strip adjustment and ALS calibration that is provided by laser scanner manufacturers, e.g., RiProcess (Riegl), Attune (Leica), or LMS (Optech). Friess has published a rigorous method that represents these industry-driven developments [26]; however, other publications of this branch can rarely be found.

C. Our contribution

The majority of related work is focused on ALS campaigns that are organized in parallel flight lines for area-wide airborne surveying (strip adjustment). Typically, it is assumed that the

laser scanner is operated in the nadir view on a fixed-wing aircraft. This kind of ALS measurements follows a standard procedure that can be thoroughly planned ahead of each survey, including the ability to prepare a network of ground-based GNSS reference stations [5].

Commercial ALS systems that are used for airborne surveying are typically calibrated based on data that are captured at certain calibration sites. Usually, these calibration sites include a number of known objects and ground control points. In contrast, our workflow allows ALS calibration at arbitrary, previously unknown urban terrain, without any need to prepare or arrange special calibration objects.

The experiments described in Section IV consisted of applying the proposed procedures to recorded raw data in a post-processing mode. Up to now, our experimental ALS system has not allowed immediate data access. However, we expect that the proposed methods can be accomplished in real-time on an operational system. The work shown here especially addresses support for short-term operations, such as the surveillance of urban areas [27], terrain-referenced navigation [28], or rapid change detection [29]. Examples can be found in assistance systems for helicopter pilots, obstacle avoidance, landing operations in urban terrain, search and rescue missions (SAR), emergency services, or disaster management. These applications lead to different requirements for ALS data acquisition. Consequently, the described methodology of data analysis adapts to extended boundary conditions:

--An oblique forward-looking ALS sensor is used instead of (or in addition to) the classical nadir configuration.

--Although optimal conditions are assumed when calibrating the ALS system, it is possible to run into GNSS problems during the actual helicopter mission, for instance, the SPS mode (Standard Positioning Service), adverse satellite constellation, or loss of GNSS signals.

Even though the proposed workflow adopts some ideas presented in related work (calibration based on identification and matching of planar features), it differs in detail as it applies to these altered circumstances. For instance, strong emphasis is put on segmentation methods that are suited to the conditions of oblique data acquisition. Moreover, the segmentation results are reusable to support subsequent applications such as change detection. Attributes that are mostly invariant to point distribution and density are derived from principal component analysis, e.g., area, centroid, orientation, and moments of inertia. These attributes are evaluated to associate planar shapes found in different overlapping data sets. Pairs of homologous planes are first used to estimate the system's boresight parameters. Remaining discrepancies between the corrected point clouds are then attenuated by a data-based registration of corresponding surfaces. In both cases, a new method to transfer the planarity constraints into systems of linear equations is presented. The following statements outline our contribution:

--The proposed registration and calibration methods are based on attributes that are unaffected by varying point density, as it is encountered due to oblique view and altering directions of flight.

--The approach presented in this work uses a new and efficient method to exploit planarity constraints. It is not limited to a specific scanning principle and can be applied to a large variety of laser scanners and other (future) 3D sensors.

--The proposed rigid-body registration method is reliable even in case of considerable offsets (e.g., those caused by GNSS dropouts).

--No special calibration arrangement is required to determine the ALS boresight correction. Consideration of rooftops and facades in overlapping point clouds results in sufficient statistical variation of planar features.

--Tests were successfully performed for widely different types of urban areas (e.g., large cities, suburban terrain, and small villages).

--The methods are feasible to be used for in-flight calibration on an operational system.

--Attributes used during the calibration and registration process can be further exploited to support object-based change detection.

The paper is organized as follows. Section II describes the components that are commonly used for ALS data acquisition, the principles of airborne laser scanning, and typical problems occurring in direct georeferencing. All necessary processing methods are presented in Section III. We start with a summary of common issues in handling of irregularly distributed point clouds. Then, a RANSAC-based shape extraction method is described. After feature extraction and matching of homologous surfaces, we derive the boresight calibration parameters of the sensor system. We then provide an accurate alignment of the corrected ALS data sets. A description of our ALS setup and experimental results can be found in Section IV. Finally, Section V presents a brief discussion and our conclusions.

II. PRINCIPLES OF AIRBORNE LASER SCANNING

Typically mounted tightly on an aircraft, an ALS system comprises a laser scanning device and an inertial navigation system together with a GNSS receiver. Reference data of several base stations are normally used to achieve the best possible accuracy when measuring the aircraft's absolute position, either in real-time (RTK, Real-Time Kinematic) or during post-processing (PPK, Post-Processed Kinematic). Synchronously, the inertial navigation system measures the aircraft's pitch, roll, and heading angles. The laser scanner is the core element of the ALS system. It generates and deflects single laser pulses, for which it measures the time-of-flight to receive an echo caused by one or more objects within the laser footprint. Taking the speed of light into consideration, the system is able to determine the distance between the aircraft and the reflecting object. Knowing the aircraft's position and orientation as well as the scanning geometry, the absolute position of the point illuminated by the laser pulse can be determined. Fig. 1 illustrates our configuration, which can be considered as a typical ALS setup, despite the fact that we mostly used an oblique forward-looking laser scanner ($30° \leq \varphi \leq 60°$). A detailed description of our specific ALS system can be found in Section IV.A, or more thoroughly in [30].
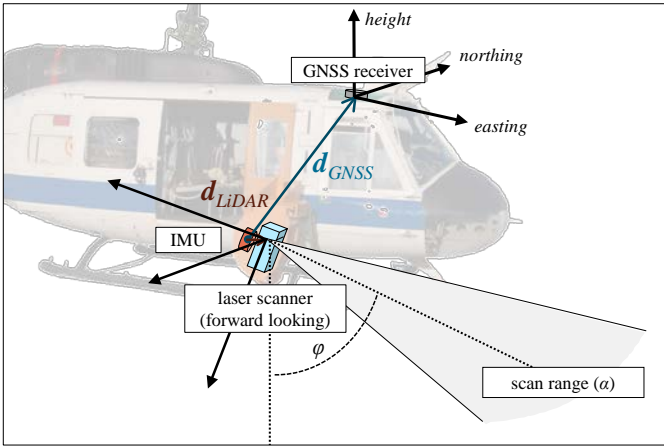
Fig. 1. Exemplary ALS sensor carrier and configuration: laser scanner, GNSS receiver, and IMU installed on a helicopter (specific lever arms).

A. Direct georeferencing

Because the ALS system consists of several spatially separated parts, the mutual placement and alignment of these elements is of great importance when combining the complementary information of all components. Generally, the lever arms (d_{LiDAR}, d_{GNSS}) of the laser scanner, GNSS receiver and IMU can be determined with sufficient accuracy once the system is assembled, where "sufficient" means that remaining errors are negligible compared to other influences. While metering the aircraft's position and orientation, the lever arms are taken into account to transfer positional coordinates to the laser scanner's center. These calculations are usually done within the control unit of the navigational sensor system, which uses a Kalman filter to fuse the GNSS and IMU channels. The laser scanner itself makes use of the time-of-flight distance measurement principle, for example, by estimating the range ρ_L corresponding to the first echo pulse found by constant fraction discrimination or full waveform analysis. Typically, opto-mechanical beam scanning provides a specific scan pattern, in which the distance $\rho_L(t)$ measured at time t is georeferenced according to the scanning geometry as well as the position and orientation of the sensor. With the navigational information p_N and R_N relating to the laser scanner's center (according to the lever arms), $\rho_L(t)$ is directly georeferenced in the following way[1]:

$$p_L(t) = p_N(t) + R_N(t) \circ R_S(t) \circ r_L(t). \qquad (1)$$

Equation (1) is given with the following notations:

$p_N(t)$: the 3D position of the laser scanner at time t in a Cartesian geographic coordinate system, e.g., UTM (Universal Transverse Mercator) coordinates.

$r_L(t)$: the distance measured by the laser scanner, given as a Euclidean vector $(0, 0, \rho_L(t))^T$.

$R_S(t)$: a 3×3 rotation matrix that describes the relative orientation of the scanning mechanism and the scanning process, i.e., the current direction of laser pulse emission.

$R_N(t)$: a 3×3 rotation matrix that describes the orientation

---

[1]Throughout this paper, the symbol ∘ denotes the standard matrix multiplication, whereas · represents the vector dot product.

---

of the laser scanner in 3D space.

$p_L(t)$: the geocoordinates of the resulting "laser point".

The aggregated points $p_L(t)$ acquired within a time interval $[t_1, t_2]$ are usually called a "LiDAR point cloud" or, more specifically, a "LiDAR strip" (in the case of a straight line flight trajectory).

B. Sources of errors

Direct georeferencing of laser range measurements provides a data acquisition method that is appropriate for airborne surveying (e.g., of urban areas). However, the accuracy of the derived 3D point clouds is affected by several influencing factors, reflecting the complexity of the ALS system. In addition to the varying exactness of the navigational information sources, several systematic effects can lead to reduced point positioning accuracy. Exemplary limiting factors are the scanning precision and range resolution of the specific laser scanning device. Other negative effects can be introduced by inaccurate synchronization of the system components. Significant offsets are caused by mounting errors or disregarded lever arms (displacements between laser scanner, IMU, and GNSS antenna). Potential error sources have been investigated by Schenk [31] and Filin [32]. With regard to specifications of the components in our ALS system, the contribution of each error source to the point positioning error in a distance of 500 meters is listed in Table I.

TABLE I
OVERVIEW OF ERROR SOURCES

error source	point positioning error in a distance of 500 m
geodetic datum conversion	<1 cm
GNSS related errors (PPK or RTK)	3-30 cm
IMU related errors (angular accuracy)	10-20 cm
synchronization/interpolation	3-5 cm
ranging accuracy (full-waveform scanner)	2-3 cm
footprint size	10-20 cm
scanning performance	3-5 cm
lever arms	2-3 cm
boresight misalignment	>100 cm

C. Boresight alignment

A few of the potential errors listed in Table I are responsible for white noise, which stochastically affects the point positioning accuracy. The majority of influences will cause systematic shifts and nonlinear distortions of the resulting point clouds. Among these systematic errors, the IMU/laser misalignment usually has the highest impact on the overall precision. Unlike their relative position, the exact relative orientation of the IMU and the laser scanner cannot be determined directly with the necessary precision. Generally, it is recommended to rigidly mount both devices to avoid changes in the boresight alignment due to vibrations or temperature effects. Anyhow, even in case of rigid mounting,

the initial boresight misalignment is typically of the order of some tenths of an angular degree. This misalignment corresponds to point positioning errors of several meters in a distance of 500 meters. The alignment of both components will change each time the system is reassembled, unless the IMU is a built-in part of the laser scanner.

Contrary to all other influencing factors, the boresight misalignment cannot be corrected properly in an independent way. Instead, the relative orientation of the IMU and the laser scanner must be taken into consideration during direct georeferencing:

$$\boldsymbol{p}_L(t) = \boldsymbol{p}_N(t) + R_N(t) \circ R_B \circ R_S(t) \circ \boldsymbol{r}_L(t) . \qquad (2)$$

As mentioned before, the IMU/laser alignment is typically incorrect by some tenths of an angular degree. We account for this by introducing a rotation matrix R_B in (1). In Section III, we outline a workflow to determine R_B automatically while acquiring multi-aspect ALS data of an urban terrain.

III. STRATEGY FOR DATA PROCESSING

A reasonable approach to estimate R_B in (2) could start with an identification of homologous points $\boldsymbol{p}_L(t_1)$ and $\boldsymbol{p}_L(t_2)$ in overlapping parts of the point clouds. With regard to (2), we would then be able to determine the proper boresight alignment that minimizes the Euclidean distance for all such point pairs. Unfortunately, due to irregular sampling, it is unrealistic to expect the occurrence of such homologous points. A similar problem also arises in ICP methods, where it is solved, for instance, by examining point-to-(tangent) plane instead of point-to-point distances [20].

We adapt this idea to recover the boresight angles and, at the same time, we take into account that we analyze the data of an urban area. Data points that are most likely to result in correct point-to-plane assignments are those collected at man-made objects, such as facades and the rooftops of buildings. Consequently, we apply filtering techniques to detect points that represent such objects and distinguish them from others (e.g., vegetation). Moreover, we exclude the ground level because this widespread subset of points would otherwise slow down the segmentation of proper localized planar surfaces. Following plane fitting, we match several attributes derived from planar shapes to find correct plane-to-plane correspondences. Finally, R_B is determined on the basis of data points associated with these homologous planar surfaces.

A. Data structures

An adequate data structure is needed to store, query, and analyze three-dimensional point clouds. ALS data sets typically consist of up to several millions or billions of irregularly distributed 3D points, for which it is important to have an appropriate indexing. Otherwise, even simple queries would require traversing of the entire point cloud. Different methods of efficient 3D data handling can be found in literature. Conveniently, a digital surface model (DSM) is generated by sampling the 3D points onto a 2D grid. Data sets handled this way are usually referred to as 2.5D data. These data can be examined using image processing methods.

However, a simple 2D rasterization is an improper data structure when dealing with full 3D point clouds, e.g., those originating from multi-aspect ALS scans. For instance, points measured at the facades of buildings are suppressed when these data are assigned to horizontal raster cells.

Octrees and k-d trees [33] are widely used in computer graphics and geometric modeling. These data structures are well-suited for indexing of large point sets and other spatial data. The volume containing the entire point cloud is recursively divided into subspaces by introducing splitting planes perpendicular to the coordinate axes. The recursive refinement of this mesh can be represented by a tree-like hierarchical decomposition. When implementing an octree, fixed octants are utilized for space partitioning. In contrast, a k-d tree uses splitting planes, which are adaptive to varying point density. After arranging the data in this way, search operations can be performed very efficiently by using the tree properties to quickly eliminate large portions of the search space. We use k-d tree data structures (k=3) for most of the search operations and data processing methods that are described in the next sections. In addition to the Cartesian coordinates $\boldsymbol{p}_L$ of each laser point, attributes such as echo width and amplitude are associated with elements of the point cloud. Moreover, each point's origin is stored, i.e., its timestamp t, the measured range $\boldsymbol{r}_L$, and the scanning geometry R_S. Sensor positions and orientations $\boldsymbol{p}_N(t)$ and $R_N(t)$ are interpolated from the synchronously recorded GNSS/IMU information, which is typically captured with a frequency lower than the pulse repetition rate.

B. Local principal component analysis (PCA)

In the context of airborne laser scanning, data processing methods usually aim at the filtering and clustering of complex point clouds, the classification of points, as well as the segmentation of objects and structures. Extracting features in the local neighborhood of each element is a good starting point for further analysis. Hoppe *et al.* demonstrated the practical usability of covariance analysis to estimate local properties of point-sampled surfaces [11]. Let $\boldsymbol{p}_i$ denote a given 3D point in the point cloud P. Its neighboring points $\boldsymbol{p}_{ij}$ can be found efficiently by traversing the k-d tree of P and identifying all points that fall below a predefined distance r to $\boldsymbol{p}_i$. The radius r of the bounding sphere is chosen globally according to the average point density so that these vicinities are likely to contain a significant number of points. When analyzing ALS point clouds, values assigned to r typically lie between 0.5 and 5 meters. With a quantity n of neighboring points, $\boldsymbol{p}_{i0}=\boldsymbol{p}_i$, and $\bar{\boldsymbol{p}}$ being the centroid of $P_i=\{\boldsymbol{p}_{i0},\boldsymbol{p}_{i1},...,\boldsymbol{p}_{in}\}$, the covariance matrix C is given by the following expression:

$$C = \left(\boldsymbol{p}_{i0} - \bar{\boldsymbol{p}},...,\boldsymbol{p}_{in} - \bar{\boldsymbol{p}}\right) \circ \left(\boldsymbol{p}_{i0} - \bar{\boldsymbol{p}},...,\boldsymbol{p}_{in} - \bar{\boldsymbol{p}}\right)^{\mathrm{T}} . \qquad (3)$$

The 3×3 covariance matrix C is symmetric and positive semi-definite; therefore, its eigenvalues λ_1, λ_2, and λ_3 are real-valued, non-negative numbers. The eigenvectors $\boldsymbol{v}_1$, $\boldsymbol{v}_2$, and $\boldsymbol{v}_3$ of C are the principal axes of P_i. Each eigenvalue λ_k, divided by the number of points (n+1), gives a normalized measure of the scatter in direction of the respective eigenvector $\boldsymbol{v}_k$. The

result of covariance analysis can be interpreted as an ellipsoid of inertia, which is given by the orthogonal vectors $\lambda_1 v_1$, $\lambda_2 v_2$, and $\lambda_3 v_3$. The eigenvalues of C are commonly indexed in such a way that $\lambda_1 \leq \lambda_2 \leq \lambda_3$. If λ_1 is near zero, and it is significantly smaller than λ_2 and λ_3, it indicates a locally planar region, and v_1 represents a good approximation of the surface normal. We perform these computations for every point p_i in P. In each case where we can find enough neighboring points and the eigenvalues reveal local planarity, the normal direction $n_i = v_1$ or $n_i = -v_1$ is assigned to point p_i and we state that p_i is of class **A**. Otherwise, p_i is assigned to class **B**. To guarantee consistent normal directions, the orientation of n_i is chosen to satisfy $(R_N \circ R_S \circ r_L) \cdot n_i \leq 0$. Remarkably, local PCA is not sufficient to identify continuous planar surfaces, and points acquired at smooth non-planar surfaces are also assigned to class **A**. This identification is handled in the next two sections.

C. Region growing

It is often desirable to identify coherent regions within the point cloud data. The basic idea of region-based segmentation is to expand a point set that is initialized with a single point q_i. Starting from this seed point, a measure of similarity $d(q_i, q_k)$ is evaluated for all neighboring points q_k within a bounding volume around q_i. Depending on the search criteria, similarity is typically defined by attributes such as the echo amplitude, height above ground, or normal direction. Points q_k are added to the region if $d(q_i, q_k)$ falls below a certain threshold d_{max}, which indicates that these points have similar attributes. This procedure is repeated recursively with all new points in the increasing region, until no more additional points are found. Several parameters have substantial influences on the result of region growing:

--the seed point q_i is either selected manually or found by an automatic procedure,

--the threshold d_{max} is chosen locally or globally,

--the measure of similarity d must be carefully set to push the region growing into the right direction, which ends up in the requested results. The measure d is evaluated either locally or by comparing to the original seed point.

In our workflow, we include a region growing technique with the aim of ground level segmentation. To find appropriate seed points automatically, sections of the point clouds are identified in which the histogram of height values clearly shows a multimodal distribution. There, laser points at ground level appear as the lowest distinct peak. Starting from such locations, we locally collect low-lying points that fall below a certain slope, and we assign these points to class **G**. This way, some outliers in the point cloud (e.g., those caused by multiple reflections) are treated as ground level, but these outliers do not affect the result as we use multiple seed points. In this example, the local measure of similarity is given by the following:

$$d(p_j, p_k) = \frac{\text{height}(p_k) - \text{height}(p_j)}{\|p_j - p_k\|}. \tag{4}$$

An exemplary threshold would be $d_{max} = 0.25$. The necessary

search operations are accomplished by means of the k-d tree data structure. In general, this method may misclassify some points (e.g., inner courtyards), but this misclassification is negligible for our application. An overview of advanced methods for bare-earth extraction can be found in [34].

D. RANSAC-based detection of planar shapes

The random-sample-consensus (RANSAC) paradigm as described by Fischler and Bolles is a standard technique to estimate parameters of a mathematical model underlying a set of observed data [8]. It is particularly used in cases where the observed data contain data points that can be explained by a set of model parameters (inliers) and data points that do not fit the model (outliers). To apply the RANSAC scheme, a procedural method has to be available that determines the model parameters based on a minimal subset of the data.

Schnabel *et al.* have demonstrated the efficiency of RANSAC techniques to extract shapes in unorganized point clouds [9]. In our approach, we utilize this robust parameter estimation to identify planar regions in the ALS data. If we have a set S of points $\{p_1, \ldots, p_n\}$ and we assume that this set mostly contains points that approximately lie on one plane (inliers) and some others that do not (outliers), simple least-squares model fitting would lead to poor results because the outliers would affect the estimated parameters. However, several robust techniques other than RANSAC are available for robust regression in such situations, e.g., iteratively reweighted least squares (IRLS). Instead of using weighting factors, RANSAC estimates a plane by taking only the inliers into account, provided that the probability of choosing only inliers among the data points is sufficiently high. To compute a plane, we select a random sample of three non-collinear points (the minimal subset) p_i, p_j, and p_k. The resultant plane's normal vector n_0 is computed as $n = (p_i - p_j) \times (p_i - p_k)$, $n_0 = n/\|n\|$, and with $(x - p_i) \cdot n_0 = 0$, the plane's Hessian normal form is obtained. Using this representation, we can evaluate whether other points p in S are inliers or outliers simply by computing the distance $|(p - p_i) \cdot n_0|$ to the previously obtained plane. If this distance falls below a pre-defined threshold, we assess that point as inlier. The number of inliers and the average distance of all inliers to the plane are used to evaluate the quality of the fitted plane. This procedure is repeated several times to converge towards the best fitting plane.

Application to ALS data of urban terrain

In this subsection, we propose a method for automatic ALS point cloud analysis that is an iterative combination of RANSAC plane fitting and point-specific region growing. The procedure is intended to detect planar objects, such as parts of buildings, and separate these from clutter objects, such as bushes or trees. A complete overview of the algorithm is shown in Table II. During initialization, overlapping point clouds (e.g., multi-aspect or multi-temporal data) are cropped to tiles that contain the urban area of interest (overlap area). For each such tile, a separate k-d tree is generated, the ground level is segmented, and local principal components are computed. Details of these steps {**1**}-{**3**} are described in the previous sections.

TABLE II
ALGORITHM: DETECTION OF PLANAR SHAPES

{1}	Generate a *k*-d tree data structure to handle search operations in the point cloud *P* (see Section III.A).
{2}	Perform a local principal component analysis at each point p_k in *P*. Depending on the results, p_k is either assigned to class **A** or class **B** (see Section III.B). Points of class **A** obtain a normal direction n_k.
{3}	Filter out (most of the) points at ground level (see Section III.C). Let P_{nG} denote the set of remaining non-ground points.

outer loop / inner loop / region growing:

{4}	Choose an unprocessed point p_i of class **A** among the data points in P_{nG}.
{5}	Check a sphere of radius *r* around p_i for adjacent points of class **A**. Include these in a new set *S* if their associated normal direction is similar to that of p_i.
{6}	Set the inner loop counter *m* to zero.
{7}	If *S* contains more than a specific number of points, increase the counter *m* by one. Otherwise mark point p_i as discarded and go to step **{17}**.
{8}	Perform a RANSAC-based plane fitting to the 3D points in the specified set *S* (see Section III.D).
{9}	If the number of inliers is low, mark p_i as discarded and go to step **{17}**.
{10}	Fit a plane to the inliers in a least squares sense and obtain the plane's Hessian normal form $E{:}(x-p){\cdot}n_0=0$
{11}	Push p_i on a stack ("last in, first out" data structure).
{12}	Pop the first element p_j off the stack.
{13}	Check each point p_k in a sphere of radius *r* around p_j, which has not already been looked at, whether it lies sufficiently near to the plane *E*, meaning that $d(p_k)=|(p_k-p){\cdot}n_0|\leq \varepsilon$. If so, include the point p_k in a new set *S'*. If additionally p_k is of class **A** and $|n_0{\cdot}n_k|\approx1$ indicates a match of normal directions, push p_k on the stack.
{14}	While the stack is not empty, go to **{12}**. Otherwise continue with step **{15}**.
{15}	If the counter *m* has reached its predefined maximum (e.g. three cycles), mark all points in *S'* as processed, extract features of this planar region (see Section III.E) and go to step **{17}**. Otherwise continue with **{16}**.
{16}	Go to step **{7}** with the new set of points *S:=S'*.
{17}	Repeat from **{4}** until all selectable points are processed.

The algorithm successively fits planes to the data points, wherever this is possible. In each run of the outer loop, we select an unprocessed point of class **A** in the point cloud *P*. A planar shape is likely to be found at such a location. In the following steps, we try to fit a plane to the neighboring data points at that position. The RANSAC technique provides a robust estimation of the plane parameters, together with an automatic evaluation of the quality (e.g., number of inliers). If the fitted plane is of poor quality, we assess the data associated with the current location as clutter. Otherwise, we try to optimize the plane fitting by looking for all data points that support the obtained plane. The underlying operation is accomplished in steps **{12}**, **{13}**, and **{14}**, which represent a region growing algorithm. During region growing, points of classes **A** and **B** are treated in different ways. Only points of class **A** are able to expedite the region growing, if their positions and associated normal directions (from principal component analysis) are consistent with the plane parameters. This condition avoids jumps across different planar regions. In the inner loop, local plane fitting and region growing are repeated (e.g., two times) using all the supporting points to get a more accurate result. A typical application is depicted in Fig. 2. We use this algorithm to identify points that form the facades and rooftops in the ALS data of an urban area.
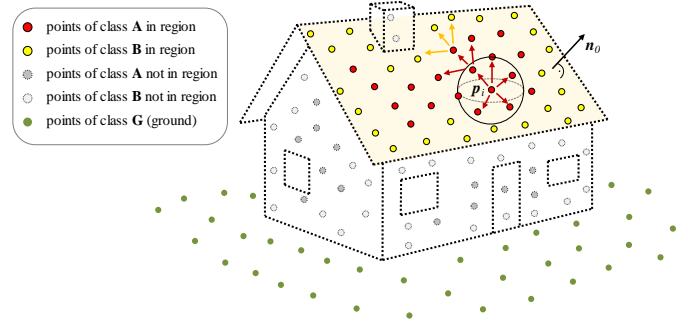

Fig. 2. Extraction of planar shapes using RANSAC-based parameter estimation and point-specific region growing.

E. Feature extraction and matching

In the following sections, we distinguish between different situations that involve ALS data registration. In the first case, an ALS database of the urban area is built from scratch by operating the same airborne sensor system on overlapping flight lines with an oblique forward looking laser scanner (multi-aspect data, Subsection III.F.1). In the second case, we align current data to a reference, for example, for change detection (multi-temporal data, Subsection III.F.2). Both types of boundary conditions allow the determination of the boresight correction R_B if errors related to GNSS positioning can be reduced to a minimum. This error reduction is achieved by applying the reference data from a network of ground-based GNSS stations (RTK or PPK). However, if a helicopter is equipped with a calibrated ALS sensor system, 3D laser data can be used to support the pilot, for example, by providing flight guidance, terrain-referenced navigation [28], or on-line change detection. In these scenarios, we expect low positioning accuracy (SPS) or even GNSS dropouts that lead to offsets of several meters, depending on the quality of the specific IMU in use. To handle these situations, we propose a rigid-body registration method that is reliable even in case of considerable offsets (Section III.G). In all these three cases, a robust matching technique is used, as explained in this section.

To assign identical planar shapes across two different ALS point clouds or overlapping tiles of the same data set, we

derive several geometric attributes and evaluate distances of feature vectors. When applying the procedure described in Section III.D, clusters C of points $\{c_1,…,c_n\}$ are found which represent planar shapes (e.g., the rooftop in Fig. 2). Similar to the attributes defined in Section III.B, the following attributes are used to characterize each cluster C:

   --the centroid $\bar{c}$ of C, which is the arithmetical average of all points in $\{c_1,…,c_n\}$,

   --the normalized and sorted eigenvalues $(\underline{\lambda}_1,\underline{\lambda}_2,\underline{\lambda}_3)$ $=(\lambda_1,\lambda_2,\lambda_3)/n$ of the covariance matrix $(C-\bar{c})\circ(C-\bar{c})^T$,

   -- the unit normal direction n_0, which is the eigenvector v_1 corresponding to the smallest eigenvalue λ_1.

These descriptive attributes are computed in each point cloud and for every cluster of coplanar points. Given such a planar shape C_a in point cloud P_A, we search for a matching counterpart C_b in data set P_B. First, the displacement of the centroids has to fall below a maximum distance (e.g., 25 m). We limit search operations to this search radius after organizing the centroids into an efficient data structure (see Section III.A). Second, the angle between the normal directions should be small (e.g., smaller than 15°, meaning that $|n_{0a}\cdot n_{0b}|>0.966$). Third, the normalized eigenvalues of the respective covariance matrices should be similar. With $\underline{\lambda}_a=(\underline{\lambda}_{a,1}, \underline{\lambda}_{a,2}, \underline{\lambda}_{a,3})$, we try to verify the following:

$$\frac{\left\|\underline{\lambda}_a - \underline{\lambda}_b\right\|}{\left\|\underline{\lambda}_a\right\|+\left\|\underline{\lambda}_b\right\|} \le \varepsilon_1 \quad (\text{e.g. } \varepsilon_1 = 0.1), \tag{5}$$

$$\left|\frac{\lambda_{a,2}}{\lambda_{b,2}} + \frac{\lambda_{b,2}}{\lambda_{a,2}} + \frac{\lambda_{a,3}}{\lambda_{b,3}} + \frac{\lambda_{b,3}}{\lambda_{a,3}} - 4\right| \le \varepsilon_2 \quad (\text{e.g. } \varepsilon_2 = 0.05). \tag{6}$$

Both equations describe distance measures to compare $\underline{\lambda}_a$ with $\underline{\lambda}_b$. Equation (5) represents the Euclidean distance of these vectors in relation to an average of their magnitude. This normalization ensures that (5) is scale independent in terms of area size and measuring unit. In (6), we compare component-by-component ratios of the nonzero components of $\underline{\lambda}_a$ and $\underline{\lambda}_b$. In the case of an equal shape of C_a and C_b, each such ratio of normalized eigenvalues is close to one, and therefore, (6) is close to zero. Additionally, (6) is not susceptible to small variations in shape because $d(x+x^{-1})/dx=0$ for $x=1$. Pairs of planes that comply with these conditions are considered homologous. However, wrong assignments may occur especially in case of considerable offsets and a large search radius. To be robust against these perturbations, the procedures described in the next sections are supplemented with a RANSAC scheme. Based on some tests with real sensor data, we estimated the typical number of inliers among all assignments in cases where only the centroids were compared (case A). In addition, the normal directions were evaluated (case B), and also (5) and (6) were considered (case C). For search radii of (5 m, 10 m, 50 m), we found the following percentage of inliers in case A: (92%, 50%, 6%), case B: (95%, 93%, 34%), case C: (95%, 95%, 80%). These numbers confirm that the necessity of the above feature assignment method mainly depends on the search radius. For instance, if

discrepancies smaller than 5 m are expected, it is sufficient to match the centroids without considering other attributes. However, in Section III.G, we also address situations of low positioning accuracy (SPS) or GNSS dropouts. These situations require a notably larger search radius, and there, the proposed feature assignment has its rightful place.

F. Boresight calibration

As introduced in the previous section, we will first present ALS calibration methods that can be applied if high-precision GNSS data (RTK or PPK) are available. In this case, the absolute positioning of the sensor can be quite accurate (3-30 cm) [35]. As opposed to an ICP method that aligns different point clouds directly by matching closest points, we use the results of plane segmentation to calibrate the boresight angles of the ALS system. In the case of criss-crossing (i.e., orthogonal and antiparallel) flight paths, discrepancies between overlapping data sets (multi-aspect, multi-temporal) are minimized by aligning homologous planar surfaces. This approach is mostly independent from discrete sampling and varying point density of the point clouds. The resulting 3D data are georeferenced to a global coordinate system.
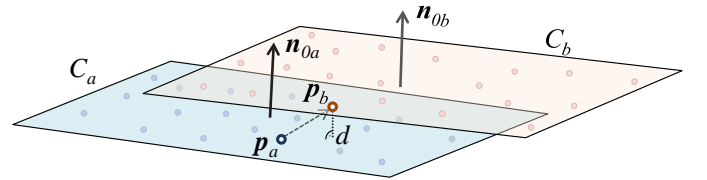

Fig. 3. Pair of homologous planar shapes C_a and C_b with representative points p_a and p_b.

1) Multi-aspect ALS data acquired by the same sensor

Again, C_a denotes a cluster of coplanar points in point cloud P_A, and C_b refers to its corresponding planar shape in data set P_B. Furthermore, let p_a denote a data point representing C_a, and let p_b denote an element of C_b (Fig. 3). Following the motivation presented in the introduction of Section III, we minimize the point-to-plane distance instead of the point-to-point distance of p_a and p_b. The main advantage of the preceding filtering and segmentation of proper localized planar shapes is the option to choose almost arbitrary representative points p_a and p_b. Even random selections and combinations are feasible. However, it is not realistic to choose all possible pairs of points because this would lead to a huge number of equations. In (9), the point-to-plane distance is derived based on a normal vector that is estimated using the biased point coordinates. To keep the impact of slightly wrong normal directions small, we choose points p_b in C_b with minimum Euclidean distance to given points p_a. However, in experiments, we found that even choosing pairs p_a and p_b with maximum Euclidean distance had only marginal impact on the results.

Points p_a and p_b are recorded at time t_a and t_b, respectively. By using these indices, direct georeferencing of p_a and p_b with regard to (2) can be written as the following expressions:

$$\begin{aligned} p_a = p_L(t_a) = p_{Na} + R_{Na} \circ R_B \circ R_{Sa} \circ r_{La}, \\ p_b = p_L(t_b) = p_{Nb} + R_{Nb} \circ R_B \circ R_{Sb} \circ r_{Lb}. \end{aligned} \tag{7}$$

We abbreviate the measured range values including their associated scanning geometry as $s_{La}=R_{Sa} \circ r_{La}$ and $s_{Lb}=R_{Sb} \circ r_{Lb}$. For any three-component vector $v=(v_1, v_2, v_3)^\mathrm{T}$, let $\chi(v)$ denote the following skew-symmetric matrix:

$$\chi(v) = \begin{pmatrix} 0 & -v_3 & v_2 \\ v_3 & 0 & -v_1 \\ -v_2 & v_1 & 0 \end{pmatrix}. \qquad (8)$$

For two vectors v and w, it is $\chi(v) \circ w = v \times w$. As already mentioned, the boresight angles are typically incorrect by some tenths of an angular degree. Therefore, the boresight correction R_B can be expressed in good approximation as $R_B = I_3 + \chi(\beta)$, where I_3 denotes the 3×3 identity matrix, and $\beta = (\beta_1, \beta_2, \beta_3)^\mathrm{T}$ are the three Euler angles of the rotation given in radians. This simplification linearizes (7) when solving for these angles. Once the boresight correction is taken into account during direct georeferencing, both point clusters C_a and C_b are expected to fall on the same place, and all related points should form a common planar shape. We can express this by claiming the following:

$$d = \left| (p_a - p_b) \cdot n \right| = 0 \qquad \forall \, p_a \in C_a, p_b \in C_b. \qquad (9)$$

Therein, $n = (n_{0a} + n_{0b})/\|n_{0a} + n_{0b}\|$ is an average of the nearly identical normal vectors attributed to C_a and C_b, whereby we set the directions to fulfill $n_{0a} \cdot n_{0b} > 0$. Together with (7), we get the following:

$$\left(p_{Na} + R_{Na} \circ R_B \circ s_{La} - p_{Nb} - R_{Nb} \circ R_B \circ s_{Lb} \right) \cdot n = 0 . \qquad (10)$$

Except for the three unknown boresight angles, measurements relating to all other parts of (10) are available. Thus, with $R_B = I_3 + \chi(\beta)$, we can rearrange this linear equation to estimate β. From (10), we obtain the following:

$$\left(R_{Na} \circ \chi(\beta) \circ s_{La} - R_{Nb} \circ \chi(\beta) \circ s_{Lb} \right) \cdot n = $$
$$\left(p_{Nb} + R_{Nb} \circ I_3 \circ s_{Lb} - p_{Na} - R_{Na} \circ I_3 \circ s_{La} \right) \cdot n . \qquad (11)$$

Now we can transform the left side of this equation:

$$\left(R_{Na} \circ \chi(\beta) \circ s_{La} - R_{Nb} \circ \chi(\beta) \circ s_{Lb} \right) \cdot n = $$
$$\left(R_{Na} \circ (\beta \times s_{La}) \right) \cdot n - \left(R_{Nb} \circ (\beta \times s_{Lb}) \right) \cdot n = $$
$$(\beta \times s_{La}) \cdot \left(R_{Na}^T \circ n \right) - (\beta \times s_{Lb}) \cdot \left(R_{Nb}^T \circ n \right) = $$
$$\det\left(R_{Na}^T \circ n, \beta, s_{La} \right) - \det\left(R_{Nb}^T \circ n, \beta, s_{Lb} \right) = \qquad (12)$$
$$\left(s_{La} \times \left(R_{Na}^T \circ n \right) \right) \cdot \beta - \left(s_{Lb} \times \left(R_{Nb}^T \circ n \right) \right) \cdot \beta = $$
$$\left(\chi(s_{La}) \circ R_{Na}^T \circ n - \chi(s_{Lb}) \circ R_{Nb}^T \circ n \right)^T \circ \beta .$$

If we combine (11) and (12), we get the following:

$$\left(\chi(s_{La}) \circ R_{Na}^T \circ n - \chi(s_{Lb}) \circ R_{Nb}^T \circ n \right)^T \circ \beta = \qquad (13)$$
$$\left(p_{Nb} + R_{Nb} \circ s_{Lb} - p_{Na} - R_{Na} \circ s_{La} \right) \cdot n .$$

Equation (13) is of type $F \circ \beta = g$ so that elements p_a and p_b of homologous planar shapes C_a and C_b in overlapping point clouds P_A and P_B contribute a row to matrix (F, g). Typically, more than two overlapping point clouds are acquired. Pairwise matches of planar shapes across these tiles are accumulated in (F, g). For example, if a plane is contained in four overlapping data sets, it would allow six groups of matches to contribute to (F, g). The resulting over-determined linear system can be solved in a least-squares sense. To increase the robustness against wrong assignments, we supplement the solution process with a RANSAC scheme. In other words, we repeatedly select three random rows $(F_\mathrm{rand}, g_\mathrm{rand})$ in the over-determined system, derive $\beta^* = (F_\mathrm{rand})^{-1} \circ g_\mathrm{rand}$ as a preliminary solution, and evaluate the residuals $|F \circ \beta^* - g|$ to identify inliers and outliers. After some iterations, we consider only the best set of inliers $(F_\mathrm{in}, g_\mathrm{in})$. Additionally, weighting factors $w = \lambda_2 + \lambda_3$ are used when inverting the normal equations, causing larger shapes to have a higher impact on the result. We obtain

$$\beta = \left(F_\mathrm{in}^T \circ W \circ F_\mathrm{in} \right)^{-1} \circ F_\mathrm{in}^T \circ W \circ g_\mathrm{in} \qquad (14)$$

with a diagonal matrix W containing the associated weighting factors w. Finally, the boresight correction R_B is represented by the Euler angles $(\beta_1, \beta_2, \beta_3)$.

2) Existing control surfaces

In this subsection, we consider boresight calibration in the case of an existing reference (e.g., control surfaces). To allow for system calibration, we intend to align current ALS data to this reference. Again, we imply that precise GNSS data are available. The boundary conditions to determine the boresight alignment R_B are slightly different from the initial situation we had before.

Let C_d be a cluster of coplanar points in the newly acquired point cloud P_D. Again, we exploit the attributes described in Section III.E to identify corresponding planar patches in the reference data set P_M. Let C_m denote such a matching counterpart of C_d. Furthermore, let $\bar{p}_m$ be the centroid of C_m, n_{0m} the associated normal direction, and let p_d denote an arbitrary element of C_d. The direct georeferencing of this point is expressed in the following way:

$$p_d = p_L(t_d) = p_{Nd} + R_{Nd} \circ R_B \circ R_{Sd} \circ r_{Ld} . \qquad (15)$$

When considering the boresight correction R_B, all points that form the shape C_d are expected to be coplanar with C_m, which is stated by the following expression:

$$\left(p_d - \bar{p}_m \right) \cdot n_{0m} = 0 \qquad \forall \, p_d \in C_d . \qquad (16)$$

With $s_{Ld} = R_{Sd} \circ r_{Ld}$, we combine these equations and get the

following:

$$\left(\boldsymbol{p}_{Nd} + R_{Nd} \circ R_B \circ \boldsymbol{s}_{Ld} - \bar{\boldsymbol{p}}_m \right) \cdot \boldsymbol{n}_{0m} = 0 \,. \qquad (17)$$

Similar to (12)-(13), we rewrite (17) to solve for the boresight angles $\boldsymbol{\beta} = (\beta_1, \beta_2, \beta_3)^{\mathrm{T}}$:

$$\left(\chi(\boldsymbol{s}_{Ld}) \circ R_{Nd}^{\mathrm{T}} \circ \boldsymbol{n}_{0m} \right)^{\mathrm{T}} \circ \boldsymbol{\beta} = \left(\bar{\boldsymbol{p}}_m - \boldsymbol{p}_{Nd} - R_{Nd} \circ \boldsymbol{s}_{Ld} \right) \cdot \boldsymbol{n}_{0m} \,. \quad (18)$$

Analogous to our approach in the previous subsection, (18) is of type $F \circ \boldsymbol{\beta} = \boldsymbol{g}$ so that elements $\boldsymbol{p}_d$ of C_d in point cloud P_D contribute a row to matrix $(F, \boldsymbol{g})$, if C_d is associated with a planar shape C_m in the reference data set P_M. Again, we determine the Euler angles β_1, β_2, and β_3 of R_B by solving this system of linear equations with a RANSAC estimation technique, which is followed by a weighted least-squares minimization based on the inliers.

G. Rigid-body alignment of multiple point clouds

Apart from mismatches that are caused by an incorrect boresight alignment, other sources of errors may have significant influences on the fitting accuracy of multiple overlapping point clouds. In addition to high-quality ALS data acquisition, we address applications that require real-time data analysis under adverse GNSS conditions [28]. Typical examples can be found in airborne monitoring for law-enforcement purposes, disaster management, and medical or other emergency services. Moreover, it is desirable to assist helicopter pilots with obstacle avoidance and aircraft guidance in case of poor visibility conditions, during landing operations, or in the event of GNSS dropouts. In such situations, comparison of current ALS scans to existing geo-referenced 3D data could be used for terrain-referenced navigation or on-line change detection.

Despite the operation of a thoroughly calibrated ALS system, different laser point clouds still show discrepancies of some centimeters up to several meters, depending on the actual positioning accuracy of the GNSS subsystem. To resolve this problem, we perform a data-based registration of these data sets. Due to our preparatory work, we can draw on the results of plane segmentation to align 3D point clouds of urban terrain, rather than starting an ICP approach. Again, let C_d denote a cluster of coplanar points in the ALS data set P_D, which is associated with a planar shape C_m in the reference point cloud or model P_M. The Hessian normal form of the respective planes is given by the centroids $\bar{\boldsymbol{p}}_d$, $\bar{\boldsymbol{p}}_m$ and the normal directions $\boldsymbol{n}_{0d}$, $\boldsymbol{n}_{0m}$. Fig. 4 illustrates exemplary pairs of corresponding surfaces. The offset in position and orientation indicates the inaccuracy of the navigational data. We determine a rigid transformation $(R, \boldsymbol{t})$ to correct these discrepancies. Even in case of GNSS gaps, the relative exactness provided by the IMU ensures consistent ALS measurements over limited periods of time [35]. Thus, we can assume that errors of orientation would not exceed the range of $\pm 5°$. This information allows us to approximate the rotation matrix as $R = I_3 + \chi(\boldsymbol{\gamma})$, with small Euler angles $\boldsymbol{\gamma} = (\gamma_1, \gamma_2, \gamma_3)^{\mathrm{T}}$. Because associated planes should coincide after the

registration, $\bar{\boldsymbol{p}}_d$ is moved to have zero distance to the plane defined by C_m. Additionally, with both normal vectors normalized to the same half-space, $\boldsymbol{n}_{0d}$ is rotated to be identical with $\boldsymbol{n}_{0m}$. We express this by means of the following two equations:

$$\begin{aligned} \left(R \circ \bar{\boldsymbol{p}}_d + \boldsymbol{t} - \bar{\boldsymbol{p}}_m \right) \cdot \boldsymbol{n}_{0m} &= 0, \\ \left(R \circ \boldsymbol{n}_{0d} \right) \cdot \boldsymbol{n}_{0m} &= 1. \end{aligned} \qquad (19)$$

The rotation angles $\boldsymbol{\gamma} = (\gamma_1, \gamma_2, \gamma_3)^{\mathrm{T}}$ and the translation components $\boldsymbol{t} = (t_1, t_2, t_3)^{\mathrm{T}}$ are the six unknowns to be determined. To solve for these variables, we rearrange (19) and find the following:

$$\begin{aligned} \left(\chi(\bar{\boldsymbol{p}}_d) \circ \boldsymbol{n}_{0m} \right) \cdot \boldsymbol{\gamma} + \boldsymbol{n}_{0m} \cdot \boldsymbol{t} &= \left(\bar{\boldsymbol{p}}_m - \bar{\boldsymbol{p}}_d \right) \cdot \boldsymbol{n}_{0m}, \\ \left(\chi(\boldsymbol{n}_{0d}) \circ \boldsymbol{n}_{0m} \right) \cdot \boldsymbol{\gamma} &= 1 - \boldsymbol{n}_{0d} \cdot \boldsymbol{n}_{0m} \end{aligned} \qquad (20)$$

Each corresponding pair of planar patches (C_d, C_m) yields two linear equations of type (20), therefore at least three pairs have to be identified in the data to compute the rigid transformation $(R, \boldsymbol{t})$. In general, much more correspondences can be found in urban areas. These correspondences allow us to robustly estimate the rotation and translation parameters by a combination of a RANSAC scheme with a weighted least-squares approximation, similar to the approach we used in Section III.F. Finally, R is set to a proper rotation matrix with the three Euler angles $\boldsymbol{\gamma}$, and each point $\boldsymbol{p}$ in P_D is transferred to $\boldsymbol{p}_{\mathrm{new}} = R \circ \boldsymbol{p} + \boldsymbol{t}$. This transformation aligns P_D to P_M.
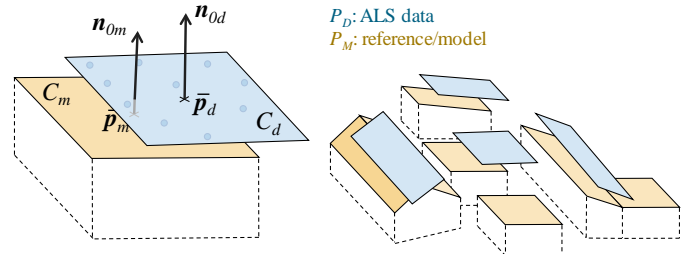

Fig. 4. Exemplary pairs of homologous planes in point cloud P_D and reference/model P_M.

IV. EXPERIMENTS

A. Experimental setup and data acquisition

As already mentioned, our current experimental ALS system lacks on-line data access. The experiments described in this section were conducted in a post-processing mode based on recorded raw data. However, we expect that an efficient implementation of the proposed methods can work in real-time on an operational system.

The data that we analyzed during this study were collected in field campaigns in the years 2006-2009, using the equipment that is briefly described below. A thorough description of the sensor system can be found in [30]. All sensors were attached to a helicopter of type Bell UH-1D. Fig. 1 shows details of the installation: the GNSS antenna is placed on top of the cockpit, whereas the laser scanner and IMU are mounted alongside on a common sensor carrier. This platform

TABLE III
TEST SITES AND DETAILS OF EXPERIMENTS

test site	coordinates WGS84	date mm/dd/yy	aspects	points (overlap)	density [pts/m²]	sensor position error RMS [cm]			PPK
						north	east	down	
Munich (TUM)	N 48° 8.94', E 11° 34.04'	10/09/06	4	3,100,000	9.7	~400	~400	~800	no
		09/02/09	4	4,400,000	5.2	1-20	1-7	1-14	yes
Rendsburg	N 54° 17.94', E 9° 41.28'	04/22/08	5	5,400,000	18.6	3-8	3-8	4-15	yes
Ruschberg	N 49° 37.18', E 7° 17.33'	09/01/09	3	4,200,000	17.7	3-10	2-7	4-13	yes
Abenberg	N 49° 14.50', E 10° 57.80'	04/18/08	4	5,400,000	16.1	2-4	2-3	3-4	yes
		08/31/09	4	6,200,000	21.1	2-3	2-3	3-4	yes
Kiel	N 54° 19.41', E 10° 8.38'	04/23/08	6	6,600,000	9.9	3-30	3-12	4-30	yes
Ettlingen (IOSB)	N 48° 56.83', E 8° 24.65'	09/01/09	3	5,000,000	20.0	3-10	3-5	3-8	yes

can be tilted in the pitch direction to allow different perspectives, i.e., the nadir or oblique view (inclination angle φ).

The RIEGL LMS-Q560 (2006) laser scanner uses the time-of-flight distance measurement principle with a pulse repetition rate of 100 kHz. The laser pulses are deflected by a rotating polygon mirror perpendicular to the direction of flight, resulting in successive scan lines and continuous sampling of the underlying terrain by the forward-moving helicopter. Multiple range values r_L under a scan angle α are identified based on a Gaussian decomposition of the full-waveform LiDAR information [3]. In our experiments, we used the sensor manufacturer's RiANALYZE software to perform this step during off-line data processing. Furthermore, waveform analysis contributed the echo width and amplitude as additional attributes. With our configuration and settings, each scan line typically covered a field of view of 60° subdivided into 1000 angular steps $\Delta\alpha$. Besides raw data conversion, no other sensor specific software tools were used because we want to keep the presented workflow configurable, extendable, and adaptable to other types of laser scanners and new 3D sensors, which we intend to analyze in future studies.

The Applanix POS AV 410 comprises a GNSS receiver (GPS) and the gyro-based inertial measurement unit (IMU), which is the main part of the inertial navigation system. The GNSS and IMU data are fused within the position and orientation computing system (PCS), delivering navigational information at a frequency of 200 Hz. Each time the inclination angle of the sensor platform in our ALS system was changed, the gimbal orientation (i.e., the GNSS/IMU lever arm) was measured automatically by a rotary position encoder. This parameter was forwarded to the PCS, and it was kept unchanged during and in good time before the actual ALS measurements, so the GNSS/IMU integration was able to adapt to each new setting. Moreover, the stability of the continuous GNSS/IMU integration was verified during post-processing. In addition to the standard navigation solution (SPS, Coarse/Acquisition mode) we used specialized software for accurate post-processing of the recorded navigational raw data. Applanix POSPac MMS incorporates the use of multiple GNSS reference stations and the import of precise satellite ephemeris information. In our experiments, we obtained these additional data from the "Satellite Positioning Service of the German State Survey" (SAPOS).

Some details about the field campaigns and the data acquisition are given in Table III. This list includes the exact coordinates of each test site, the date of the measurements, the number of intersecting flight lines at these positions, and the point density in the respective overlap area. Additionally, post-processing of the navigational data yielded estimates of the GNSS/IMU positioning errors. These variables were determined by the POSPac MMS software as a function of time, which is influenced by satellite geometry, SAPOS data, Kalman filtering, and so forth. In Table III, separate intervals of the estimated position errors are specified for the north, east, and down (NED) direction at each test site.

An oblique forward-looking sensor configuration was used in most of our experiments. Typically, the forward-looking angle of the sensor platform was chosen to reach about $\varphi=45°$ while flying with the helicopter's nose pitched down. Due to aviation security reasons, the minimum flight level had to be restricted to 2000 ft over cities (Munich and Kiel) and 1000 ft at sparsely populated urban regions (Ettlingen, Rendsburg, Abenberg, and Ruschberg). In the latter case, these boundary conditions led to laser strips with a width of 500 m and an average point-to-point distance of 0.5 m. Each test site was approached in a cross pattern, resulting in overlapping point clouds that show the underlying urban terrain from multiple aspects. This flight configuration is not really indispensable when it comes to the ability to recover the boresight angles. The main motivation to consider the oblique view instead of the nadir view was discussed in Sections I.A and I.C. The proposed methods are not limited to cross flight lines. However, enough data overlap is crucial for the calibration process, and sufficient variation is needed in terms of plane orientations and viewing directions. In case of an oblique forward-looking sensor, this variation is best achieved by a multi-intersecting flight path. As an example, the trajectory of the ALS system during acquisition of the "Munich (TUM) 2006" dataset is plotted in Fig. 5a. Fig. 5b shows a rendered visualization of the combined point cloud emerging from pass 1-4 in this particular case (all four directions/tiles). Additionally, Fig. 5c shows the width if a single strip at "Abenberg 2008", and it demonstrates the very different types

of urban areas we are dealing with. Each 3D point in these figures is colored according to its associated intensity, as derived from full waveform analysis (echo amplitude). Similarly, Fig. 6a depicts a close-up view of a single point cloud out of the "Ruschberg 2009" measurements, overlaid with a wire-frame model of two buildings at this location. Even though the sensor positions were measured with high accuracy (PPK), overlapping point clouds show discrepancies of several meters if the boresight alignment is incorrect. This fact is demonstrated in Fig. 6b and 6c. The graphs show a comparison of 3D points in the vertical and horizontal cross sections of two buildings in the overlap area (Hauptstr. 31). The influences of boresight misalignment were quantified and eliminated by the methods described in Section III.
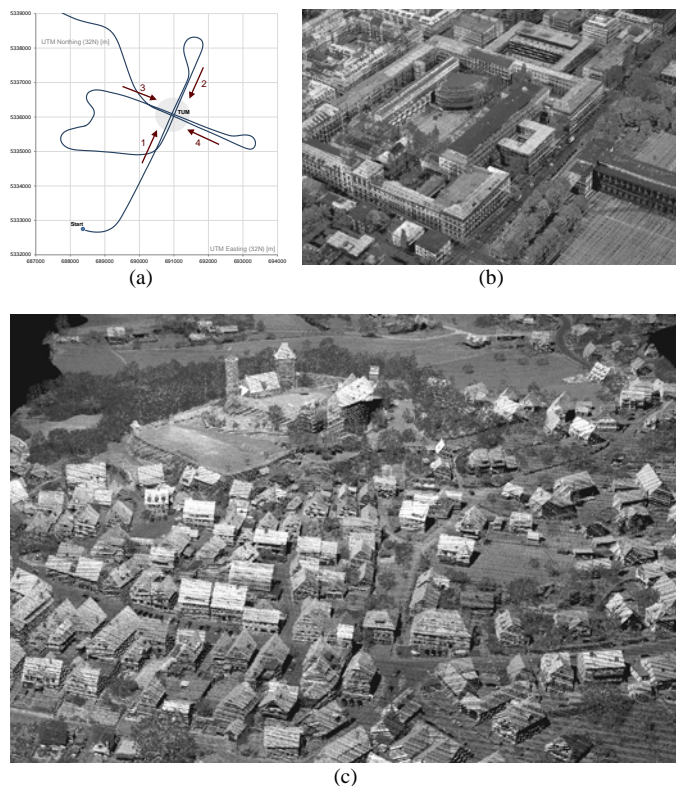

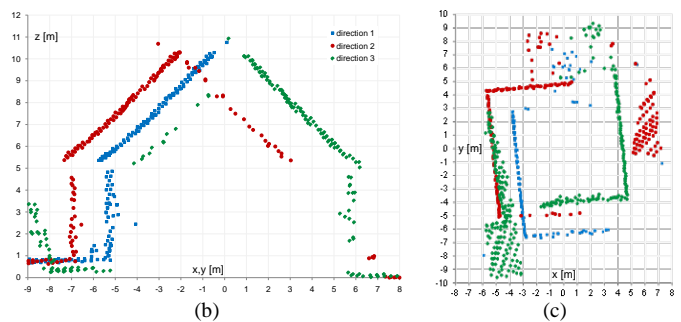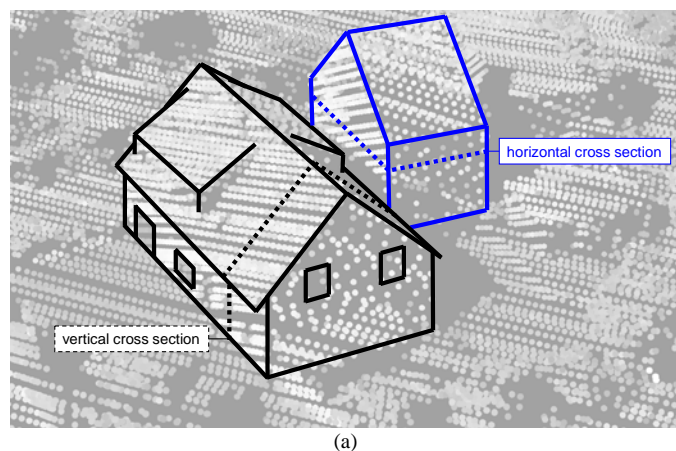(b)   (c)

Fig. 6. Close-up view of the "Ruschberg 2009" data set: (a) wire-frame model and position of sectional planes, (b) aggregated data in a vertical cross section, (c) horizontal cross section.

TABLE IV
CONTRIBUTION OF SUBROUTINES TO COMPUTATIONAL EFFORT

step in the processing chain	portion of computation time
Time synchronization, interpolation of navigational data, and direct georeferencing	28 %
Generation of k-d trees with C++ ANN library and MATLAB wrapper	4 %
Ground level identification	28 %
Local principal component analysis	11 %
RANSAC-based segmentation of planar shapes	25 %
Feature extraction and matching	2 %
Boresight calibration	1 %
Data-based alignment of point clouds	1 %

(a)   (b)

(c)

Fig. 5 (a) Top view of the trajectory at "Munich (TUM)" test site in 2006, (b) partial view of 3D laser points acquired at "Munich (TUM) 2006" (pass 1-4), (c) oblique view along a single strip ("Abenberg 2008", pass 4).

(a)

B. Implementation details and runtime information

Meanwhile, compact and lightweight laser scanners are available that provide on-line scan data (e.g., RIEGL LMS-Q160). Because the proposed methods involve many search operations in 3D point clouds, it is important to use an efficient implementation of fast search structures to be real-time capable. However, at the moment, we are only considering off-line data processing, and our implementation (MATLAB) is not runtime-optimized. The reported runtime measurements only provide an overview of the different steps and their contribution to the overall runtime behavior. Recent examples of efficient ALS data processing methods can be found in literature, which have demonstrated very good performance and real-time capability, e.g., [36]. Considering increasing hardware capacity and a more efficient implementation, we expect that our methods can be accomplished during the helicopter mission. Table IV lists the contribution of each subroutine to the computation time that we observed while applying our methods to the "Abenberg 2008" data set. These data comprise APPLANIX geopositioning information and RIEGL laser scanner data originating from four flights over this urban terrain. The overlap area amounts to 500×500 m², and it was sampled by 5,400,000 directly georeferenced 3D points that were acquired within 4×20 seconds. Due to turning maneuvers of the

helicopter (cf. Fig. 5a), the whole process of data acquisition took about 11 minutes. Using the hardware and software described below, data processing was performed in a total of 28 minutes, which can be traced back to our inefficient implementation in MATLAB. The recorded raw data were preprocessed and converted to ASCII format using the sensor manufacturer's software tools POSPac MMS and RiANALYZE, respectively. Our own processing chain started after these initial steps. In this example, the data were analyzed on a standard laptop computer with an Intel Core 2 Duo P9400 2.4 GHz processor running MATLAB 2007a. To speed up the creation of the search structures, we substituted our own octree implementation with the C++ ANN library for efficient k-d tree generation [37], which makes Table IV less conclusive at this point.

TABLE V
PARAMETER SETTINGS USED FOR THE EXPERIMENTS

| Section	parameter	value
Table II {2}	radius used for local PCA threshold for class **A**	$r=3$ m $\lambda_1<0.01$
Table II {3}	max. slope (ground level)	$d_{max}=0.25$
Table II {5}	search radius similar normal directions	$r=3$ m $\|\boldsymbol{n}_s \cdot \boldsymbol{n}_i\|>0.966$
Table II {7}	min. points in S	$\#S>7$
Table II {8}	RANSAC confidence interval	0.2 m
Table II {9}	min. percentage of inliers	75%
Table II {13}	search radius threshold for point assigned to plane matching normal directions	$r=3$ m $\varepsilon=0.25$ m $\|\boldsymbol{n}_0 \cdot \boldsymbol{n}_k\|>0.966$
Table II {15}	cycles of inner loop	3
Section 3.E	search radius matching normal directions threshold (5) threshold (6)	15 m $\|\boldsymbol{n}_{0a} \cdot \boldsymbol{n}_{0b}\|>0.966$ $\varepsilon_1=0.1$ $\varepsilon_2=0.05$
Section 3.F.1)	RANSAC confidence interval	0.4 m
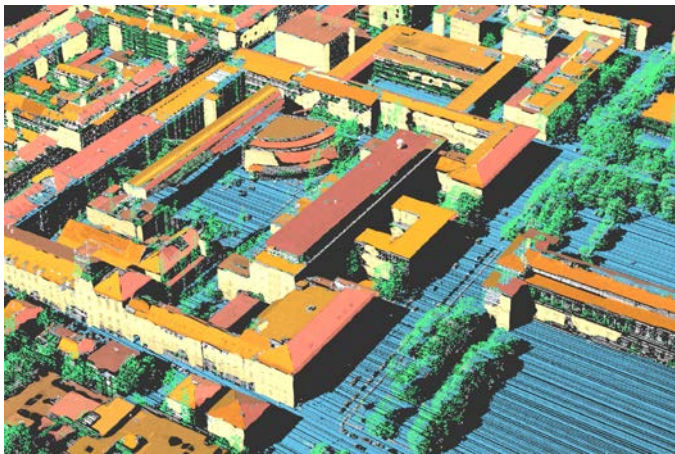
Fig. 7. Point classification and plane segmentation for "Munich (TUM) 2006" (pass 1).

C. Results

The proposed methods were applied to the data listed in Table III. Detailed parameter settings used for the experiments are given in Table V. Fig. 7 shows representative results of point classification and the segmentation of planar shapes for the first point cloud of the "Munich (TUM) 2006" measurements. Points at ground level are shown in blue, non-coplanar points are colored green, and planar shapes are shown in yellow-red color according to their specific normal direction.

The boresight angles $(\beta_1, \beta_2, \beta_3)$ of the ALS system were determined based on data of each specific proving ground. Table VI gives an overview of the results, as well as some statistics related to the number of utilized planar pairs and their orientation. Remarkably, cities like Kiel and Munich mainly showed the presence of flat roofs, whereas gable roofs were typically found in the small villages. Only 5% of the planar pairs can be ascribed to facades, which was to be expected due to fairly different viewing directions. The three boresight angles describe the misalignment of the laser scanner with respect to the IMU. With the sensor platform set to a nadir-looking configuration ($\varphi=0°$), $(\beta_1, \beta_2, \beta_3)$ would correspond to the (heading, roll, pitch) axes of the helicopter frame, but because we used an oblique forward-looking sensor (and an IMU that was rigidly mounted to it), the angles cannot be interpreted this way. Analogous to Fig. 6, Fig. 8 depicts cross sections of two buildings in the "Ruschberg 2009" data set after applying the appropriate boresight correction. When comparing the determined boresight angles in Table VI, it has to be considered that the system was reassembled each year. Nevertheless, the results found at the "Abenberg 200x" test site in both 2008 and 2009 show almost consistent values of $\beta_1=0°$, $\beta_2=0.16°$, $\beta_3=0.17°$ with variations of only ±0.01°. In both cases, we had nearly optimal conditions during the experiments. This fact hints at boresight misalignment caused by a fixed deformation of the sensor platform and/or permanent displacement of the drill-holes used for the sensor installation. In this context, the significantly smaller value of β_1 compared to β_2 and β_3 comes about by accident rather than by design. The angles arising from the "Munich (TUM) 2006" data set differ noticeably from all others, which can be ascribed to missing GNSS corrections (SAPOS) in this exceptional case. To evaluate the reliability of the respective boresight parameters, we repeated the procedure of plane segmentation, matching, and solving for $(\beta_1, \beta_2, \beta_3)$ several times for each test site. Because a large number of random operations are used within our approach (e.g., RANSAC and random seed selection for plane segmentation), the resulting standard deviations can act as an estimate of the confidence level. Additionally, in case of the "Abenberg 2009" measurements, we repeated the proposed procedures 250 times on the corrected data and found the 1σ intervals depicted in Fig. 9. Remarkably, the variation of β_2 appears to be significantly smaller than the others, a fact that is confirmed in Table VI.

At the end of our workflow, remaining discrepancies are addressed by a data-based alignment of the corrected point clouds, as described in Section III.G. Obviously, this step is

TABLE VI
RESULTS: IMU/LASER BORESIGHT ANGLES

test site	number of planar pairs, (flat roofs / gabled roofs / facades)	β_1, (σ) [°]	β_2, (σ) [°]	β_3, (σ) [°]
Munich (TUM) 2006	218, (157 / 47 / 14)	0.0837, (0.0041)	0.0039, (0.0007)	-0.1492, (0.0048)
Munich (TUM) 2009	296, (148 / 118 / 30)	-0.0132, (0.0033)	0.1762, (0.0008)	0.2102, (0.0045)
Rendsburg 2008	249, (0 / 245 / 4)	-0.0102, (0.0061)	0.1825, (0.0014)	0.1894, (0.0026)
Ruschberg 2009	116, (16 / 92 / 8)	-0.0073, (0.0041)	0.1848, (0.0010)	0.1782, (0.0019)
Abenberg 2008	320, (46 / 261 / 13)	0.0305, (0.0050)	0.1510, (0.0013)	0.1684, (0.0036)
Abenberg 2009	324, (42 / 253 / 29)	-0.0015, (0.0011)	0.1739, (0.0003)	0.1702, (0.0007)
Kiel 2008	670, (475 / 150 / 45)	-0.0190, (0.0100)	0.1632, (0.006)	0.1891, (0.0077)
Ettlingen (IOSB) 2009	60, (31 / 24 / 5)	-0.0485, (0.0032)	0.1796, (0.0009)	0.1237, (0.0018)

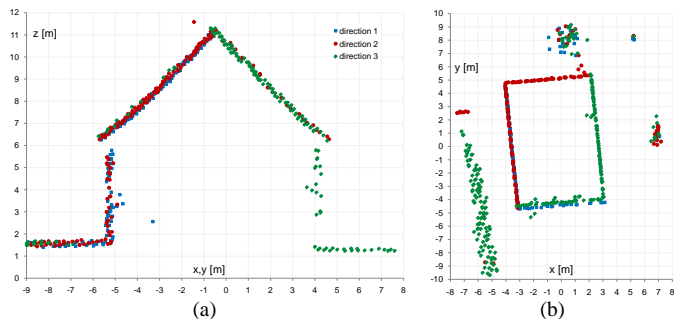optional in cases where the boresight correction led to sufficient point positioning accuracy (Fig. 8).

Fig. 8. Buildings in the "Ruschberg 2009" data set after boresight adjustment without further registration: (a) vertical cross section, (b) horizontal cross section.
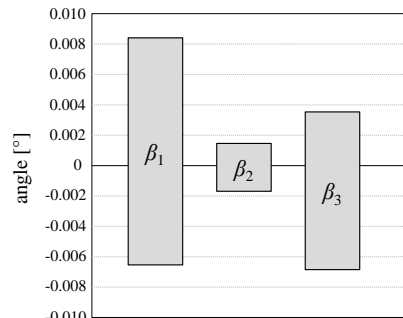

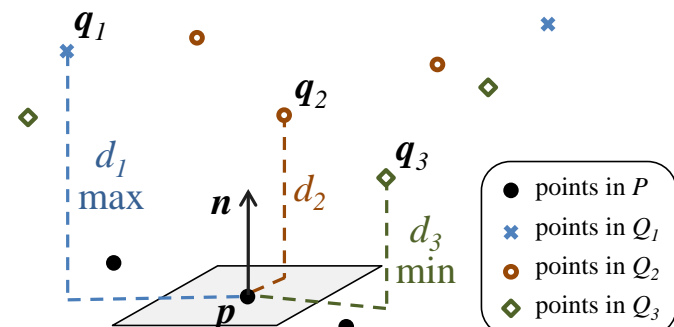Fig. 9. One-sigma intervals found for the boresight angles (after first correction).

Fig. 10. Evaluation of local discrepancies (example: 4 point clouds).

Additional computations are required to derive a quantitative measure of fitting accuracy. In the following evaluation, we derive such a measure from quantifiable local point-to-tangent plane discrepancies. First, we identify all points that are of class **A** (cf. Section III.B), including the ground level. For all such points, we look for the respective closest points in each of the other data sets. If p denotes an arbitrary point of class **A** in point cloud P, then we search for points q_i in the other (overlapping) point clouds Q_i ($P \neq Q_i$) that have minimal Euclidean distance to p:

$$\|q_i - p\| = \min_{q \in Q_i} \|q - p\| \qquad (21)$$

Because the local normal direction n at position p is known, we can estimate the particular local discrepancy to each of the other point clouds as the following:

$$d_i = \left|(q_i - p) \cdot n\right|. \qquad (22)$$

At each occurrence of a point of class **A** in any of the point clouds we obtain $\min(d_i)$ and $\max(d_i)$, describing the minimum and the maximum observed local discrepancy at this position. An example that shows four overlapping point clouds is depicted in Fig. 10. To derive a global indicator of fitting accuracy, we inspect both the entire set of minimum local discrepancies and the entire set of maximum local discrepancies. For both sets, we derive separate median values (rather than separate arithmetic means, taking into account that the local distances d_i are affected by outliers due to occlusions and non-overlapping parts of the data sets). The bars in Fig. 11 show the interval between these two median values. On average, local discrepancies of the point clouds can mainly be found in this interval. If this interval is broad, this indicates that some parts of the data are better aligned than others. The goal of calibration and registration is to shrink this interval and move it to zero. The indicators of (relative) fitting accuracy were determined for each test site on the basis of the uncorrected data, after the boresight calibration, and after the data-based registration. A confirmation of the absolute point positioning accuracy cannot be given this way because it would require independent reference data (control points, or

control patches). However, except for one test site, all results in Fig. 11 were achieved by considering post-processed GNSS information in combination with several orthogonal as well as antiparallel flight lines. Therefore, this evaluation of the boresight calibration should also reflect the accuracy of absolute georeferencing.
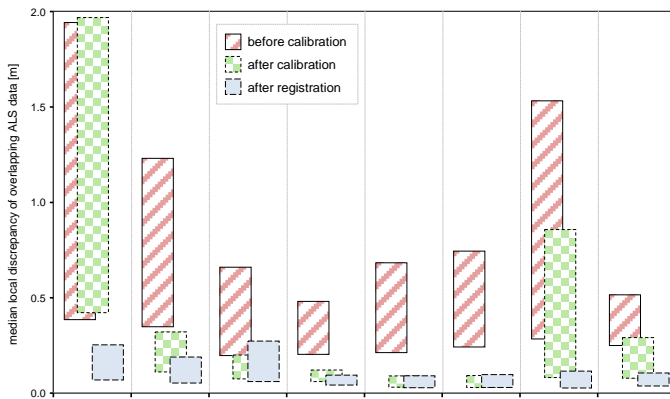

Fig. 11. Evaluation of ALS system calibration and data-based registration: bars indicating the amount of local displacements.

V. DISCUSSION AND CONCLUSIONS

In cases where multi-view and/or multi-temporal airborne LiDAR data are analyzed, considerable offsets occur that are caused by a number of potential error sources. Imperfections of the ALS sensor system and adverse conditions during data acquisition usually lead to significant discrepancies between overlapping laser point clouds. In the literature, this problem is often approached solely by data-based registration techniques (e.g., ICP methods), which sometimes improve the relative fitting accuracy, but blur the exact geographic position of the data sets. Additionally, data registration has no long-term effect on subsequent measurements.

Most of the error sources in airborne laser scanning can be reduced or avoided in an independent manner, for example, before or while assembling the ALS system. When considering accurate sensor trajectories (RTK or PPK), the IMU/laser boresight misalignment can be found as the most important remaining influence on point positioning accuracy. Our approach towards fusion and comparison of multiple point clouds integrates point classification, plane segmentation, boresight calibration, and rigid-body alignment. The proposed methods were tested with (but are not limited to) data of an oblique forward-looking line scanner. All experiments described in Section IV demonstrated usability and reliability, even with widely differing types of urban areas.

Remarkably, the boresight correction that was found for the "Munich (TUM) 2006" data set had no enhancing effect on the overall fitting accuracy. This observation can be explained by missing PPK exactness in this particular case, which led to dominant GNSS positioning errors of several meters that spoiled the calibration process. Adjusting the IMU/laser boresight this way is pointless without precise positioning accuracy.

In all other experiments, we fell back on the existing SAPOS network in Germany instead of using our own GNSS reference stations. Although the SAPOS stations delivered highly precise correction data, their distance to the actual test site often exceeded 20 km, which decreased the PPK positioning accuracy. Additionally, the satellite constellation can be a limiting factor. These facts were confirmed by the results found at the "Kiel 2008" test site, where we came across sensor position errors up to 30 centimeters (Table III). Although reasonable boresight angles were found at this test site, the fitting accuracy could only be moderately increased (cf. Fig. 11). In cases of variable GNSS positioning errors, there is an additional chance that proper planar pairs are falsely removed by the RANSAC outlier rejection, which increases the fitting accuracy for only parts of the overlapping data. This effect of over-fitting can be seen in the "Ettlingen (IOSB) 2009" example, where only a low number of planar pairs were available for the corrections. If the "Abenberg 2009" calibration parameters are applied to the "Ettlingen (IOSB) 2009" data instead, local discrepancies are almost identical to those shown in Fig. 11. This observation means that the fitting accuracy is quite low in this example even if a perfectly calibrated system is used, which hints at the presence of GNSS errors. However, the proposed rigid-body alignment method (Section III.G) is suited to attenuate relative discrepancies between overlapping tiles in such situations.

All other test sites revealed reliable and reproducible boresight angles of the ALS system that clearly improved the absolute point positioning accuracy, with almost no need for any further registration. For instance, a maximum standard deviation of $\sigma = 0.007°$ was encountered for the determined boresight angles within each of the "Abenberg 200x" data sets. However, when comparing these parameters between the different test sites, some larger variations in the boresight angles were found, even if the system was not reassembled between the measurements. Besides possible over-fitting due to GNSS errors, this fact hints at some additional phenomena that affected our data. Some possible influences can be assumed to be specific to our hardware. Even under optimal post-processing conditions, the absolute angular accuracy of the Applanix POS AV 410 system is specified with 0.008° for the roll and pitch angles, and 0.025° for the heading angle [35]. If the absolute orientation measured by the IMU/GNSS system is wrong, these angular errors are incorrectly appended to the boresight parameters. Other negative effects could have been caused by the scanning mechanism of the laser scanner, which had not been calibrated since 2006. After some rough missions and shipments of the device, an offset between the scanning plane and encoder plane might have occurred which led to effects that influence the process of boresight calibration.

Nevertheless, the consistency of results in our experiments demonstrates that the fitting accuracy is significantly improved once boresight parameters are found, and the system is kept unchanged. The maximum and minimum local discrepancies shown in Fig. 11 were reduced to at least twenty percent of the values found for the uncalibrated system. For instance, remaining point offsets at "Abenberg 200x" amount to 3-8 cm.

These average offsets are close to the statistical scatter, which can be ascribed to other influences listed in Table I, but also to the roughness of the underlying planar objects (e.g., roofs). However, maximum remaining offsets were observed at the boundary of the laser strips, which can only be explained by additional phenomena such as those mentioned above.

Once the correct boresight angles are determined, the associated rotation matrix R_B can be used for subsequent direct georeferencing with respect to (2), as long as the system is not reassembled. According to Fig. 11, we achieved the best results in the case of the "Abenberg 200x" measurements. This can be explained three ways. First, we had nearly optimal GNSS/PPK conditions during these experiments, with estimated sensor position errors of only 3 cm (Table III). Second, the flight level was comparatively low at this test site, causing angular errors to result in smaller discrepancies. Third, this urban area is in fact a small village in hilly terrain, with many different roof shapes and varying building orientations (Fig. 5c). Obviously, these variations represent optimal boundary conditions to determine the boresight angles. This is particularly true if an oblique forward-looking ALS sensor is used (such as in our case), for which we recommend criss-crossing flight lines as depicted in Fig. 5a. In addition to advantages in terms of data coverage, this multi-view configuration leads to a sufficiently broad distribution of planar pairs that is needed for an accurate boresight angle determination.

After ALS system calibration and data registration, the results of point classification and shape segmentation are a useful basis for city modeling, terrain-referenced navigation, or on-line change detection. These topics will be part of our future work.

REFERENCES

[1] A. Wehr and U. Lohr, "Airborne Laser Scanning – an Introduction and Overview," in *ISPRS Journal of Photogrammetry and Remote Sensing*, vol. 54, no. 2–3, pp. 68–82, July 1999.

[2] B. Jutzi and U. Stilla, "Range determination with waveform recording laser systems using a Wiener Filter," in *ISPRS Journal of Photogrammetry and Remote Sensing*, vol. 61, no. 2, pp. 95–107, November 2006.

[3] W. Wagner, A. Ullrich, V. Ducic, T. Melzer, N. Studnicka, "Gaussian decomposition and calibration of a novel small-footprint full-waveform digitising airborne laser scanner," in *ISPRS Journal of Photogrammetry and Remote Sensing*, vol. 60, no. 2, pp. 100–112, April 2006.

[4] U. Stilla and B. Jutzi, "Waveform Analysis for Small-Footprint Pulsed Laser Systems," in *Topographic Laser Ranging and Scanning: Principles and Processing*, J. Shan and C. K. Toth, Eds. CRC Press, Boca Raton, pp. 215–234, 2008.

[5] P. Rieger, "The Vienna laser scanning survey," in *GEOconnexion International Magazine*, pp. 40–41, May 2008.

[6] T. Rabbani, S. Dijkman, F. van den Heuvel, G. Vosselman, "An integrated approach for modelling and global registration of point clouds," in *ISPRS Journal of Photogrammetry and Remote Sensing*, vol. 61, no. 6, pp. 355–70, February 2007.

[7] G. Vosselman, B. G. H. Gorte, G. Sithole, T. Rabbani, "Recognising structure in laser scanner point clouds," in *International Archives of Photogrammetry, Remote Sensing and Spatial Information Sciences*, vol. 46, no. 8, pp. 33–38, October 2004.

[8] M. A. Fischler, R. C. Bolles, "Random sample consensus: a paradigm for model fitting with applications to image analysis and automated cartography," in *Communications of the Association for Computing Machinery*, vol. 24, no. 6, pp. 381–395, June 1981.

[9] R. Schnabel, R. Wahl, R. Klein, "Efficient RANSAC for point-cloud shape detection," in *Computer Graphics Forum*, vol. 26, no. 2, pp. 214–226, May 2007.

[10] A. Sampath, J. Shan, "Segmentation and Reconstruction of Polyhedral Building Roofs From Aerial Lidar Point Clouds," in *IEEE Transactions on Geoscience and Remote Sensing*, vol. 48, no. 3, pp. 1554–1567, March 2010.

[11] H. Hoppe, T. DeRose, T. Duchamp, J. McDonald, W. Stuetzle, "Surface reconstruction from unorganized points," in *Proceedings of the 19th annual conference on computer graphics SIGGRAPH*, pp. 71–78, July 1992.

[12] H.-G. Maas, "Methods for Measuring Height and Planimetry Discrepancies in Airborne Laserscanner Data," in *Photogrammetric Engineering & Remote Sensing*, vol. 68 no. 9, pp. 933–940, September 2002.

[13] C. Ressl, H. Kager, G. Mandlburger, "Quality checking of ALS projects using statistics of strip differences," in *International Archives of Photogrammetry, Remote Sensing and Spatial Information Sciences*, vol. 37, no. 3b, pp. 253–260, July 2008.

[14] G. Vosselman, "Analysis of planimetric accuracy of airborne laser scanning surveys," in *International Archives of Photogrammetry, Remote Sensing and Spatial Information Sciences*, vol. 37, no. 3a, pp. 99–104, July 2008.

[15] H. Kager, "Discrepancies between overlapping laser scanner strips – Simultaneous fitting of aerial laser scanner strips," in *International Archives of Photogrammetry, Remote Sensing and Spatial Information Sciences*, vol. 35, no. B/1, pp. 555–560, July 2004.

[16] A. Habib, A. P. Kersting, K. I. Bang, D.-C. Lee, "Alternative Methodologies for the Internal Quality Control of Parallel LiDAR Strips," in *IEEE Transactions on Geoscience and Remote Sensing*, vol. 48, no. 1, pp. 221–236, January 2010.

[17] S. S. Soudarissanane, C. J. van der Sande, K. Khoshelham, "Accuracy assessment of airborne laser scanning strips using planar features, " in *Proceedings of the International Calibration and Orientation Workshop EuroCOW 2010*, Castelldefels, Spain, 6 p, February 2010.

[18] P. J. Besl, N. D. McKay, "A method for registration of 3-D shapes," in *IEEE Transactions on Pattern Analysis and Machine Intelligence*, vol. 14, no. 2, pp. 239–256, February 1992.

[19] M. Hebel, U. Stilla, "Automatic registration of laser point clouds of urban areas," in *International Archives of the Photogrammetry, Remote Sensing and Spatial Information Sciences*, vol. 36, no. 3/W49A, pp. 13–18, September 2007.

[20] S. Rusinkiewicz, M. Levoy, "Efficient Variants of the ICP Algorithm," in *Proceedings of 3D Digital Imaging and Modeling 2001, IEEE Computer Society Press*, pp. 145–152, June 2001.

[21] C. Ressl, G. Mandlburger, N. Pfeifer, "Investigating adjustment of airborne laser scanning strips without usage of GNSS/IMU trajectory data," in *International Archives of Photogrammetry, Remote Sensing and Spatial Information Sciences*, vol. 38, no. 3/W8, pp. 195–200, September 2009.

[22] A. Habib, A. Kersting, K. Bang, "Impact of LiDAR system calibration on the relative and absolute accuracy of the adjusted point cloud," in *Proceedings of the International Calibration and Orientation Workshop EuroCOW 2010*, Castelldefels, Spain, 6 p, February 2010.

[23] H. Burman, "Calibration and orientation of airborne image and laser scanner data using GPS and INS," Ph.D. dissertation, Trita-Geofoto 2000, no.11, Royal Institute of Technology, Stockholm, Sweden, 2000.

[24] J. Skaloud, D. Lichti, "Rigorous approach to bore-sight self-calibration in airborne laser scanning," in *ISPRS Journal of Photogrammetry and Remote Sensing*, vol. 61, no. 1, pp. 47–59.

[25] J. Skaloud, P. Schaer, "Towards automated LiDAR boresight self-calibration," in *Proc. 5th International Symposium on Mobile Mapping Technology*, Padua, Italy, 6 p, May 2007.

[26] P. Friess, "Toward a rigorous methodology for airborne laser mapping," in *Proceedings of the International Calibration and Orientation Workshop EuroCOW 2006*, Castelldefels, Spain, 7 p, January 2006.

[27] M. Hebel, U. Stilla, "Pre-classification of points and segmentation of urban objects by scan line analysis of airborne LiDAR data," in *International Archives of Photogrammetry, Remote Sensing and Spatial Information Sciences*, vol. 37, no. B3a, pp. 105–110, July 2008.

[28] M. Hebel, U. Stilla, "LiDAR-supported Navigation of UAVs Over Urban Areas," in *Surveying and Land Information Science, Journal of*

the American Congress on Surveying and Mapping, vol. 70, no. 3, pp. 139–149, September 2010.

[29] M. Hebel, M. Arens, U.Stilla, "Change Detection in Urban Areas by Direct Comparison of Multi-view and Multi-temporal ALS Data," in *Lecture Notes in Computer Science*, vol. 6952, Springer, pp. 185–196, October 2011.

[30] V. Schatz, "Synchronised data acquisition for sensor data fusion in airborne surveying," in *Proceedings of the 11th International Conference on Information Fusion*, pp. 1–6, Cologne, Germany, July 2008.

[31] T. Schenk, "Modeling and Analyzing Systematic Errors in Airborne Laser Scanners," in *Technical Notes in Photogrammetry*, vol. 19. The Ohio State University, Columbus, USA, 42 p, January 2001.

[32] S. Filin, "Recovery of Systematic Biases in Laser Altimetry Data Using Natural Surfaces," in *Photogrammetric Engineering and Remote Sensing*, vol. 69, no. 11, pp. 1235–1242, November 2003.

[33] J. L. Bentley, "Multidimensional binary search trees used for associative searching," in *Communications of the Association for Computing Machinery*, vol. 18, no. 9, pp. 509–517, September 1975.

[34] G. Sithole, G. Vosselman, "Experimental comparison of filter algorithms for bare-earth extraction from airborne laser scanning point clouds," in *ISPRS Journal of Photogrammetry and Remote Sensing*, vol. 59, no. 1–2, pp. 85–101, August 2004.

[35] Applanix, "POS AV Specifications," June 2009 [Online]. Available: http://www.applanix.com/

[36] P. Schaer, J. Skaloud, "Optimizing computational performance for real-time mapping with airborne laser scanning," in *Proceedings of the Canadian Geomatics Conference*, Calgary, June 2010.

[37] S. Arya, D. M. Mount, "Approximate Range Searching," in *Computational Geometry: Theory and Applications*, vol. 17, no. 3–4, pp. 135–163, December 2000.

Marcus Hebel was born in Baumholder, Germany in 1974. He received a diploma in industrial mathematics (Dipl.-Math. techn.) at the Technical University of Kaiserslautern, Germany, in 2002. From 2002 until 2009, he was with the FGAN Institute of Optronics and Pattern Recognition (FGAN-FOM), a German research establishment for defense-related studies. Since 2009, he is scientist at the Fraunhofer Institute of Optronics, System Technologies and Image Exploitation (Fraunhofer IOSB) in Ettlingen, Germany. His main research activities are sensor data fusion for helicopter applications, synthetic and enhanced vision, and analysis of laser range data.

Uwe Stilla (M'04-SM'09) was born in Cologne, Germany, in 1957. In 1980, he received a diploma (Dipl.-Ing.) in electrical engineering from Gesamthochschule Paderborn, Germany, and in 1987 he received an additional diploma (Dipl.-Ing.) in biomedical engineering from the University of Karlsruhe, Germany. From 1990 until 2004, he was with the Institute of Optronics and Pattern Recognition (FGAN-FOM) in Ettlingen, Germany. In 1993, he received his PhD (doctor of engineering) from the University of Karlsruhe with work in the field of pattern recognition. Since 2004, Uwe Stilla has a professorship at Technische Universitaet Muenchen. Prof. Stilla is head of the Department of Photogrammetry and Remote Sensing, and currently director of the Institute of Photogrammetry and Cartography. He is vice dean of the Faculty of Civil Engineering and Surveying and dean of Student Affairs of the Diploma, Bachelor's, and Master Program "Geodesy and Geoinformation" and the Master Program "Earth Oriented Space Science and Technology (ESPACE)". He has the chair of the ISPRS working group "Image Sequence Analysis", is principal investigator of the International Graduate School of Science and Engineering (IGSSE), member of the Scientific Board of German Commission of Geodesy, and member of Commission for Glaciology of the Bavarian Academy of Science and Humanities. His research focuses on image analysis in the field of photogrammetry and remote sensing. He organized several conferences on this field, edited corresponding proceedings and special issues, and published more than 250 scientific articles.